

Neutron study of the magnetism in $\text{NiCl}_2 \cdot 4\text{SC}(\text{NH}_2)_2$

N. Tsyruilin¹, C.D. Batista², V. Zapf³, M. Jaime³, B.R. Hansen¹, C. Niedermayer¹, K. C. Rule⁴, K. Habicht⁴, K. Prokes⁴, K. Kiefer⁴, E. Ressouche⁵, A. Paduan-Filho⁶, M. Kenzelmann⁷

(1) Laboratory for Neutron Scattering, Paul Scherrer Institute, CH-5232 Villigen, Switzerland

(2) Theoretical Division, Los Alamos National Laboratory, Los Alamos, New Mexico 87545, USA

(3) High Magnetic Field Laboratory, Los Alamos National Laboratory, Los Alamos, New Mexico 87545, USA

(4) Helmholtz-Zentrum Berlin, Hahn-Meitner-Platz 1, 14109 Berlin, Germany

(5) SPSMS, UMR-E CEA/UJF-Grenoble 1, INAC, Grenoble, F-38054, France

(6) Instituto de Fisica, University of Sao Paulo, 05315-970 Sao Paulo, Brazil

(7) Laboratory for Developments and Methods, Paul Scherrer Institute, CH-5232 Villigen, Switzerland

E-mail: michel.kenzelmann@psi.ch

Abstract. We study the strongly anisotropic quasi-one-dimensional $S = 1$ quantum magnet $\text{NiCl}_2 \cdot 4\text{SC}(\text{NH}_2)_2$ using elastic and inelastic neutron scattering. We demonstrate that a magnetic field splits the excited doublet state and drives the lower doublet state to zero energy at a critical field H_{c1} . For $H_{c1} < H < H_{c2}$, where H_{c2} indicates the transition to a fully magnetized state, three-dimensional magnetic order is established with the AF moment perpendicular to the magnetic field. We mapped the temperature/magnetic field phase diagram, and we find that the total ordered magnetic moment reaches $m_{tot} = 2.1 \mu_B$ at the field $\mu_0 H = 6$ T and is thus close to saturation value of the fully ordered moment. We study the magnetic spin dynamics in the fully magnetized state for $H > H_{c2}$, and we demonstrate the presence of an AF interactions between Ni^{2+} on the two interpenetrating sublattices. In the antiferromagnetically ordered phase, the spin waves that develop from the lower-energy doublet are split into two modes. This is most likely the result of the presence of the AF interaction between the interpenetrating lattices.

PACS numbers: 75.45.+j, 75.10.Kt, 75.25.-j, 78.70.Nx

1. Introduction

Low-dimensional magnets feature unusual magnetic fluctuations, which can give rise to novel ground states and collective excitations. These fluctuations are not merely the more classical deviations of magnetic moments away from the ordered direction. Low-dimensional magnets support quantum fluctuations that survive to the thermodynamic

limit and are associated with Heisenberg's uncertainty principle. Strong quantum fluctuations can also be induced by an external parameter, occurring in the vicinity to a quantum critical point (QCP) at $T = 0$ K. The presence of quantum fluctuations in the vicinity of a QCP has a strong effect on the physical properties of materials, even at finite temperature. Many of today's open problems in condensed matter physics are related to the presence of a QCP. Thus understanding these is of the utmost importance.

One of the prime examples of a QCP in low-dimensional magnets is a spin-gapped $S = 1/2$ ladder system [1] in which spins are strongly antiferromagnetically coupled along rungs. The singlet $S^z = 0$ ground state of the system is separated by a finite energy gap from the excited triplet $S^z = 0, \pm 1$. A magnetic field lowers the energy of the dispersive $S^z = 1$ excitation and closes the gap, leading to the QCP from quantum paramagnetic to the antiferromagnetically ordered state.

The field-induced AF order was first observed experimentally in the gapped $S = 1/2$ compound TlCuCl_3 [2] and explained as the Bose-Einstein condensation (BEC) of triplons [3]. The triplon condensate was also observed in many spin dimer compounds, as for example NH_4CuCl_3 [4, 5], $\text{Cs}_3\text{Cr}_2\text{Br}_9$ [6], $\text{BaCuSi}_2\text{O}_6$ [7], $\text{Cu}(\text{NO}_3)_2 \cdot 2.5\text{D}_2\text{O}$ [8], and $(\text{CH}_3)_2\text{CHNH}_3\text{CuCl}_3$ [9]. The BEC of magnetic excitations is possible in other systems as well, for example in iron based AFex_3 (A is Cs, Rb and X is Cl, Br) compounds with hexagonal arrangements of spins [10].

In contrast to spin $S = 1/2$ dimer systems, the number of pure $S = 1$ materials undergoing field-induced QCP's is scarce. A particularly interesting example is the molecule-based material dichlorotetrakis-thiourea-nickel (II) $\text{NiCl}_2 \cdot 4\text{SC}(\text{NH}_2)_2$, also known as DTN. It consists of Ni^{2+} ions carrying $S = 1$ that are located at the corners and the centers of the chemical tetragonal body-centered unit cell [11]. The magnetic lattice consists therefore of two tetragonal Ni^{2+} sublattices that are arranged in an interpenetrating fashion. The exchange interactions between neighbour spins are equal to $J_c \simeq 1.64(3)$ K and $J_{ab} \simeq 0.16(1)$ K along the crystallographic c -axis and in the ab -plane, respectively [12]. Because of strongly-interacting spins along the tetragonal c -axis, DTN can be viewed as a system of weakly-coupled $S = 1$ chains. Due to the presence of a large single-ion easy-axis anisotropy $D \sim 9$ K, a single ground state $S^z = 0$ at zero magnetic field is separated by an energy gap from the excited doublet $S^z = \pm 1$ [12, 13, 14] and the correlations between spins remain short range in the zero-temperature limit. The transition from the quantum paramagnetic to the three-dimensional long-range antiferromagnetic (AF) state occurs in the zero-temperature limit at the first critical field, which is equal to $\mu_0 H_{c1} = 2.1$ T [15]. The critical exponent $\phi = 1.5$ that is found experimentally indicates that the corresponding QCP belongs to the BEC universality class in dimension $D_{\text{PH}} = d + z = 5$ (the spatial dimension is $d = 3$ and the dynamical exponent is $z = 2$) [16, 17]. However, the spin Hamiltonian as well as the symmetry of the AF magnetic order of DTN have not been studied yet in detail using neutron scattering.

In this manuscript we present results of an in-depth investigation of magnetism in DTN using neutron scattering. We demonstrate that the ordered magnetic structure

in the field-induced AF state has collinear AF order between nearest neighbours of the Ni^{2+} sublattices, while the relative orientation between sublattices cannot be determined experimentally. The magnitude of the ordered magnetic moment as a function of magnetic field and temperature is estimated from elastic neutron scattering. We also determine the magnetic phase diagram as a function of magnetic field H and temperature T , and also as a function of the angle between the applied field and the tetragonal axis. The energy of the excited doublet at the AF zone center is investigated as a function of magnetic field. We measure the one-magnon dispersion in the fully magnetized phase of DTN, establishing the spin Hamiltonian including the strength of the inter-sublattice exchange interaction. The excitation spectrum in the antiferromagnetically ordered phase shows a splitting of the spin-wave that probably results from the interacting Ni^{2+} sublattices and the strong anisotropy.

2. Experimental details

Single crystals of DTN were grown from aqueous solutions of thiourea and nickel chloride. We performed a series of neutron scattering experiments, using the D23 and E4 diffractometers at the ILL and HZB, respectively, and the FLEX and the RITA-II cold triple-axis spectrometers at HZB and at SINQ (PSI), respectively. In the following we describe the setup of these experiments in more detail.

The ordered magnetic structure and magnetic field-temperature (HT) phase diagram with magnetic fields applied parallel to the crystallographic c -axis were studied using the thermal-neutron two-axis CEA-CRG diffractometer D23 located at ILL, France. A single crystal of deuterated DTN with dimensions $5 \times 5 \times 7$ mm was aligned with its reciprocal $(h, k, 0)$ plane in the horizontal scattering plane of the neutron diffractometer and loaded into the dilution refrigerator insert. Magnetic fields up to $\mu_0 H = 12$ T were applied along the tetragonal axis. Data were collected using neutrons with a wave length $\lambda = 1.279$ Å selected by a pyrolytic graphite Cu (200) Bragg reflection. Using a lifting-arm detector, it was possible to access Bragg reflections located away from the $(h, k, 0)$ plane. In order to determine the field-induced magnetic order, a total of 124 nuclear and 23 magnetic Bragg peaks were measured at $\mu_0 H = 6$ T.

The spin dynamics in the fully-magnetized phase of DTN was investigated at SINQ, Switzerland, using the cold-neutron three-axis spectrometer RITA2. The sample was mounted in the same way as in the D23 experiment and loaded into dilution insert. To reach the fully-magnetized phases, we used a 15 T split-coil magnet and performed the measurements at $\mu_0 H = 13.3$ T. The crystal was aligned with its reciprocal $(h, k, 0)$ plane in the horizontal scattering plane of the spectrometer and the magnetic field was applied along the c -axis. The dispersion of the low-lying excitations was mapped out through constant wave-vector scans using neutrons scattered and focused by a PG(002) analyzer with a final wave length of $E_f = 4.7$ meV.

The dependence of the magnetic phase diagram on the angle between applied field and the crystallographic c -axis was measured using the two-axis neutron diffractometer

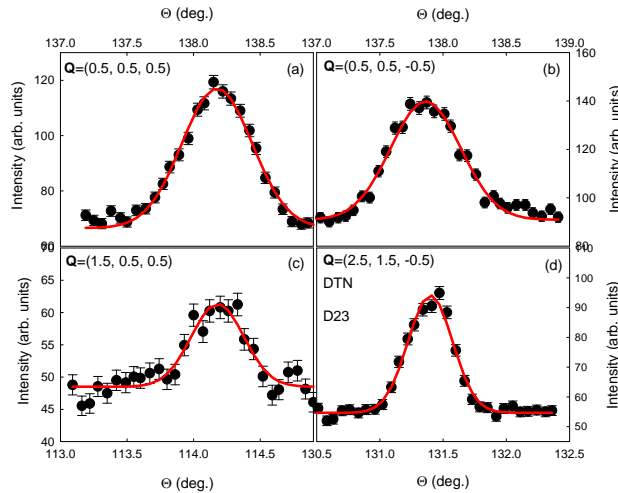


Figure 1. Magnetic Bragg peaks observed at the wave-vectors $\mathbf{Q} = (0.5, 0.5, 0.5)$, $\mathbf{Q} = (0.5, 0.5, -0.5)$, $\mathbf{Q} = (1.5, 0.5, 0.5)$ and $\mathbf{Q} = (2.5, 1.5, -0.5)$ as a function of rocking angle θ . The measurements were performed in a magnetic field $\mu_0 H = 6$ T applied along the c -axis and at temperatures $T < 50$ mK.

E4 at HZB, Germany. Four single crystals of deuterated DTN with dimensions $5 \times 5 \times 10$ mm were co-aligned with a mosaic spread less than 1° . The sample was loaded into a horizontal field magnet and aligned with its reciprocal (h, h, l) plane in the horizontal scattering plane of the instrument. PG crystals bent vertically were used as a focusing monochromator for the wave length $\lambda = 2.44$ Å. Scattered intensities were observed using a two-dimensional position-sensitive detector. The experiment was performed using a dilution refrigerator at temperatures below $T = 0.8$ K.

The wave-vector and field dependence of the spin doublet were studied using the FLEX, triple-axis spectrometer for cold neutrons at HZB, Germany. We used the same sample mount with four co-aligned crystals, a horizontal-field magnet and a dilution refrigerator as in the E4 elastic experiment. PG(002) reflections were used as monochromator and neutrons with final wave lengths of $\lambda = 5.236$ Å or $\lambda = 4.833$ Å were detected in magnetic fields up to $\mu_0 H = 6$ T. A collimation of $60'$ located after the monochromator and a cooled beryllium filter installed before the analyzer were used to suppress the beam divergence and higher-order neutron contamination. The sample was loaded into a horizontal-field magnet and aligned with its reciprocal (h, h, l) plane in the horizontal scattering plane of the instrument.

The requirement to use a horizontal-field magnet for the E4 and FLEX experiments was imposed by the following: DTN undergoes field-induced order only for sizeable magnetic fields along the tetragonal axis and the magnetic ordering vector in the AF phase is equal to $\mathbf{k} = (0.5, 0.5, 0.5)$ (see Sec. 3.1). This implies that the scattering plane of the neutron spectrometer has to be located close to the direction of the applied magnetic field. Since scattered neutrons are detected mainly in the horizontal plane of the instrument, the magnetic field thus has to be applied in the horizontal direction

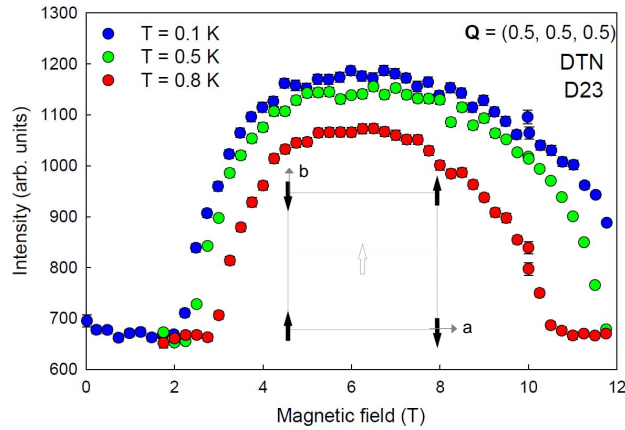


Figure 2. (Color) The neutron scattering intensities measured at the wave-vector $\mathbf{Q} = (0.5, 0.5, 0.5)$ as a function of field at three different temperatures. Inset: One of the possible ordered magnetic structure of DTN. The projections of the magnetic moments located at the corners and the center of the unit cell on the ab -plane are shown by black and white arrows, respectively.

as well. A disadvantage of any horizontal-field magnet is the limited internal space transparent to neutrons. For this reason, the E4 and FLEX experiments had limited access to the reciprocal space of the sample.

3. Results and discussions

3.1. Ordered magnetic structure

Magnetic Bragg peaks were measured in a magnetic field $\mu_0 H = 6$ T parallel to the c -axis and at temperatures $T < 50$ mK. We observed magnetic Bragg peaks at $\mathbf{Q} = (m, n, p) \pm (0.5, 0.5, 0.5)$, where m, n and p are integer numbers. The magnetic ordering vector is therefore $\mathbf{k} = (0.5, 0.5, 0.5)$.

A few of these peaks are shown in Fig. 1. The shapes of observed reflections are described by Gaussian functions. The full widths at half maximum of these Gaussians are close to the resolution limit, indicating that the system is magnetically long-range ordered. Bragg scattering was detected neither below $\mu_0 H \sim 2$ T nor above $T \sim 1.4$ K, providing strong evidence for their magnetic origin. A list of the observed magnetic Bragg peaks is given in Table. 3 in the Appendix.

The magnetic structure was refined using the program FullProf. The Appendix contains a group theoretical analysis of the possible magnetic structures. A refinement of the observed scattering intensities demonstrates that DTN has a collinear arrangement of spins within each of the Ni^{2+} sublattices in the ab -plane at $\mu_0 H = 6$ T, as shown schematically in the inset of Fig. 2. The quality of the fit of the magnetic structure is described by residual of squares $\chi^2 = 4.89$. The value of the fitted ordered magnetic moment in the ab -plane of one nickel ion is equal to $m_{ab} = 1.94(5) \mu_B$. The relative

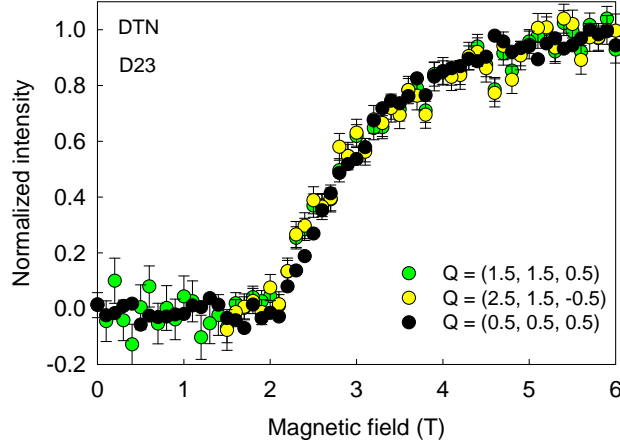


Figure 3. The scaled neutron scattering peak intensities for $T < 50$ mK measured at $\mathbf{Q} = (0.5, 0.5, 0.5)$, $\mathbf{Q} = (2.5, 1.5, -0.5)$ and $\mathbf{Q} = (1.5, 1.5, 0.5)$ are shown by black, yellow and green circles, respectively.

orientation between Ni^{2+} magnetic moments belonging to different Ni^{2+} sublattices could not be determined from the experiment. The inset of Fig. 2 shows a scenario where all the magnetic moments are collinear. Our experimental investigation directly demonstrates that the ordered magnetic components of magnetic moments in the AF phase of DTN are perpendicular to the field direction.

3.2. Magnetic phase diagram

To determine the field-temperature (HT) phase diagram of DTN, the intensity of the magnetic Bragg reflection at $\mathbf{Q} = (0.5, 0.5, 0.5)$ was measured by elastic neutron scattering as a function of magnetic field applied parallel to the tetragonal axis. Fig. 2 shows the field scans measured at $T = 0.1$ K, $T = 0.5$ K and $T = 0.8$ K. A fast growth of the AF peak intensity above the lower critical field is observed at all temperatures. After reaching the top of the "dome" located near $\mu_0 H = 6$ T, the magnetic intensities diminish slowly and finally disappear at the upper critical field H_{c2} .

The onset field of the AF phase increases with increasing temperature, consistent with the thermodynamic measurements. We also observed a decrease of the transition from the AF to a fully magnetized state with increasing temperature. The HT phase diagram seen with neutrons confirms the phase diagram obtained by specific heat and magnetocaloric effect measurements [12], particularly the asymmetry as a function of magnetic field.

To investigate a possible change in the symmetry of the magnetic structure we measured the field dependencies of different magnetic Bragg peak intensities. Fig. 3 shows the scaled peak intensities detected at the wave-vectors $\mathbf{Q} = (0.5, 0.5, 0.5)$, $\mathbf{Q} = (2.5, 1.5, -0.5)$ and $\mathbf{Q} = (1.5, 1.5, 0.5)$. The close similarity of the scaled data shows that the relative intensities of these peaks are field independent, providing evidence that

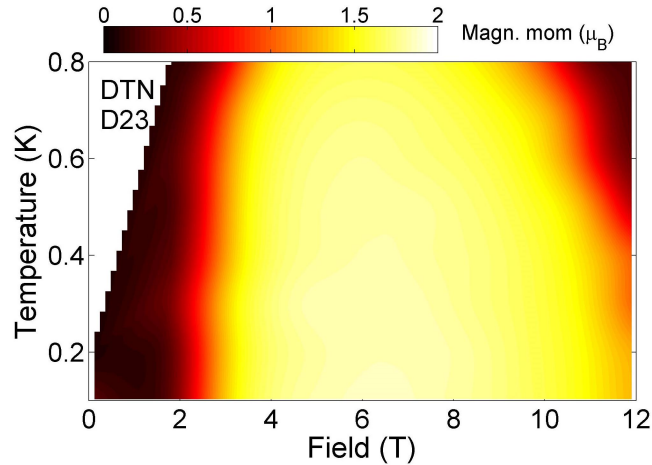


Figure 4. (Color) The AF moment ordered in the crystallographic ab -plane plotted as function of temperature and magnetic field.

the magnetic structure has the same symmetry at all points of the HT phase dome.

Since the magnetic structure does not change with field, the ordered moment is simply proportional to the square root of the magnetic Bragg peak intensity. Fig. 4 shows that the AF moment increases from zero below H_{c1} to $m_{ab} = 1.94(5) \mu_B$ at $\mu_0 H \simeq 6$ T at $T = 0.1$ K. Based on magnetization measurements [18], the ferromagnetic component of the ordered moment along the c -axis at $\mu_0 H = 6$ T is estimated to be $m_c = 0.8 \mu_B$. Hence, the total ordered magnetic moment at $\mu_0 H = 6$ T is equal to $m_{tot} = 2.1 \mu_B$. This is close to the saturation value of the fully ordered moment, $m_{sat} = 2.34 \mu_B$. The quality of the fit is independent of the momentum direction in the ab -plane, so that the exact direction of the ordered magnetic moments cannot be determined.

We also determined the magnetic phase diagram as a function of the magnetic field applied along the crystallographic a - (H_a) and c -axis (H_c). The Bragg peak intensity at the wave-vector $\mathbf{Q} = (0.5, 0.5, 0.5)$ was measured as a function of the angle between the magnetic field and the tetragonal c -axis. The accessible area of the diagram was limited by the dark angles of the horizontal-field magnet. Fig. 5 shows a colours plot of the neutron scattering intensity as a function of H_a and H_c . This plot demonstrates that the transition from a quantum paramagnetic to an AF phase occurs only if a major component of a magnetic field is applied along the tetragonal axis. Magnetic order is not observed if the angle γ between an applied magnetic field and the tetragonal axis is greater than $\sim 55^\circ$. This is a direct consequence of a strong easy-axis anisotropy: a magnetic field applied in the ab -plane acts on a linear combination of the excited states $S^z = \pm 1$, mixing them with the ground state $S^z = 0$, and thus increasing the spin gap and preventing the system from ordering. Our results independently confirm the behaviour of the first critical field as a function of field angle away from the tetragonal axis, which was previously determined by magnetostriction measurements [15, 19].

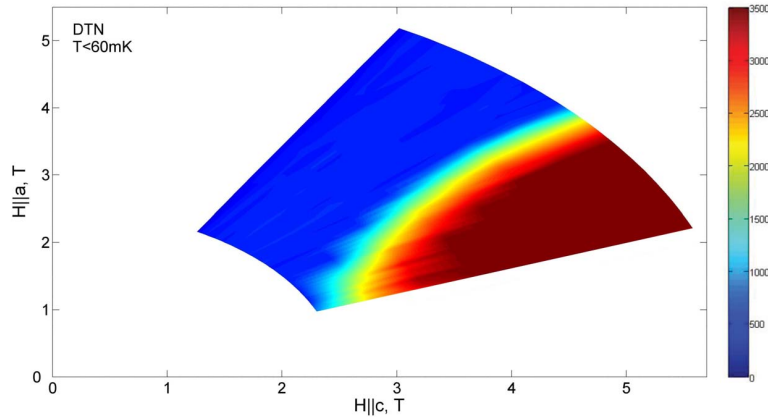


Figure 5. (Color) A colour plot of the neutron scattering peak intensity (in arbitrary units) measured at $\mathbf{Q} = (0.5, 0.5, 0.5)$ at magnetic fields up to $H = 5.5$ T applied in crystallographic a - and c -directions at temperatures $T < 50$ mK.

3.3. Magnetic Bose-Einstein condensation

To study the field-induced magnetic BEC in DTN we measured the energy of the magnetic excitations as a function of magnetic field using neutron spectroscopy. Due to the restrictions from the horizontal-field magnet, several wave-vectors such as $\mathbf{Q} = (0.5, 0.5, 0.5)$ were not accessible and the constant- \mathbf{Q} measurements were performed at $\mathbf{Q} = (1.5, 1.5, 1.5)$.

Fig. 6 shows the magnetic excitation spectrum at $\mathbf{Q} = (1.5, 1.5, 1.5)$ as a function of energy for different magnetic fields strengths. The field was always applied along the c -axis. The red lines in the energy scans represent a Gaussian function convoluted with the instrument resolution function and fitted to the data. The well-defined peak at $E = 0.285(5)$ meV that was observed at zero field splits into two peaks in the presence of a magnetic field. This is direct microscopic evidence that the zero-field magnetic excitations in DTN are doublet states. The energy of the lower doublet state decreases linearly with increasing field, while the energy of the higher doublet state increases with increasing field. The fitted slope of the decrease of the lower doublet and of the increase of the doublet are $0.139(6)$ meV/T and $0.132(3)$ meV/T - identical within the error bar.

At H_{c1} , the energy of the lower doublet is identical to that of the $S^z = 0$ ground state. These two states get mixed above H_{c1} leading to the AF long-range order that we observed by neutron scattering. Importantly, the closing of the energy gap at H_{c1} , together with a preserved rotational symmetry of spin components in the ab -plane observed in our elastic measurements, indicates that the QCP at H_{c1} in DTN can be described as a BEC QCP to a very good approximation [1].

Fig. 6(a) shows the summarized field dependence of the energy of the doublet. Due to the Zeeman effect, the energy of the higher doublet grows linearly as a function of magnetic field in the AF phase. The fitted slope of the increase of energy of the higher doublet is equal to $0.221(4)$ meV/T. This slope is almost twice as large as the

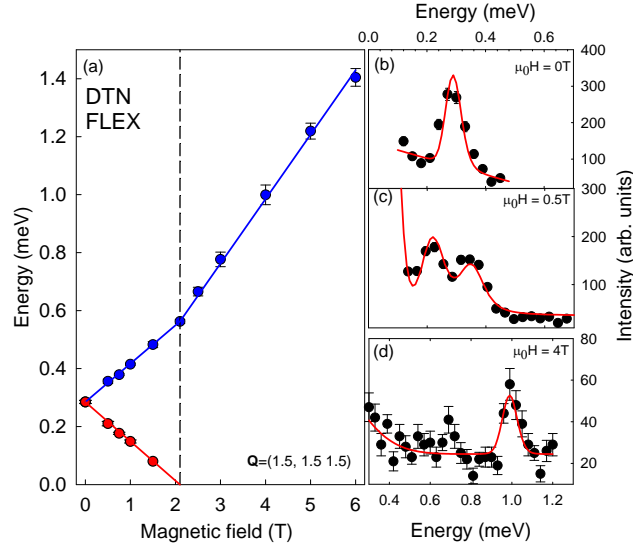


Figure 6. (a) The energy of the doublet as a function of magnetic field applied parallel to the crystallographic c -axis and measured at wave vector $\mathbf{Q} = (1.5, 1.5, 1.5)$ for $T < 50$ mK. The energy scans performed in magnetic fields $\mu_0H = 0$ T, $\mu_0H = 0.5$ T and $\mu_0H = 4$ T are shown in subplots (b), (c) and (d), respectively. For simplicity, these plots do not describe or show excitation energies of the spin-wave excitations arising from the AF order. These occur at energies below 0.8 meV depending on the magnetic field and will be discussed in detail later. An example of such an excitation is visible in (d) at $E = 0.7$ meV.

slope observed in the paramagnetic phase. This effect is a direct consequence of the field-induced lowering of the ground state energy above H_{c1} due to the mixing (linear combination) of the $S^z = 1$ and $S^z = 0$ states.

Fig. 7 shows the field dependence of the scattering at $\mathbf{Q} = (1.5, 1.5, 1.5)$ in the ordered phase. A broad peak with a width much larger than the instrumental resolution is observed between $E = 0.35$ meV and $E = 0.7$ meV in the energy scans at $\mu_0H = 4$ T and $\mu_0H = 5$ T (see Fig. 7(a-b)). Upon increase of magnetic field to $\mu_0H = 6$ T the broad scattering evolves into a better defined excitation at $E \approx 0.4$ meV as it is shown in Fig. 7(c). A width larger than the instrumental resolution possibly indicates several energy levels located close to each other. Our observation of a magnetic mode with the energy $E \sim 0.4$ meV at the AF zone center at $\mu_0H \sim 6$ T is consistent with the result of the ESR measurements [20].

3.4. Spin dynamics in the fully magnetized phase

It is possible that DTN features Ni^{2+} - Ni^{2+} interactions between corner and center cell spins. In this case, the spin Hamiltonian would be given as:

$$\hat{H} = \sum_{r,\nu} J_\nu (\kappa S_r^z S_{r+\nu}^z + S_r^x S_{r+\nu}^x + S_r^y S_{r+\nu}^y)$$

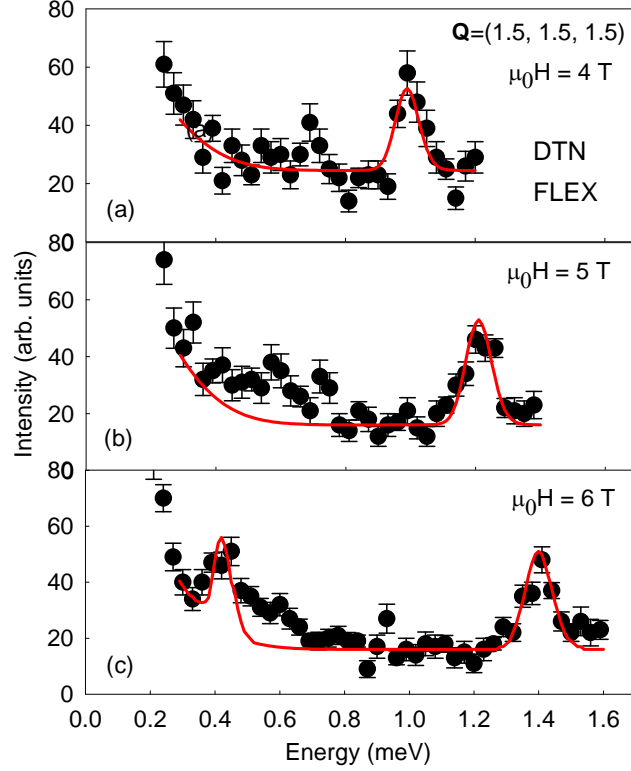


Figure 7. Energy scans for $T < 50$ mK performed at $\mathbf{Q} = (1.5, 1.5, 1.5)$ at $\mu_0H = 4$ T, $\mu_0H = 5$ T and $\mu_0H = 6$ T are shown in (a), (b) and (c), respectively. The solid lines are fits of long-lived spin-wave excitations broadened by the resolution function.

$$+J_f \sum_{r,\nu'} S_r \cdot S_{r+e_{\nu'}} + D \sum_r (S_r^z)^2 - g\mu_B H \sum_r S_r^z, \quad (1)$$

where

$$e_{\nu} = \{\hat{\mathbf{a}}, \hat{\mathbf{b}}, \hat{\mathbf{c}}\},$$

$$e_{\nu'} = \left\{ \frac{\hat{\mathbf{c}}}{2} \pm \frac{\hat{\mathbf{a}}}{2} \pm \frac{\hat{\mathbf{b}}}{2} \right\}.$$

Here κ describes the possibility of an exchange anisotropy and J_f is the exchange interaction between two tetragonal spin sublattices. The latter interaction was not considered in a previous neutron scattering study of DTN [12].

The parameters of the spin Hamiltonian (Eq. 1) can be determined best in the fully magnetized phase of DTN. This is because the spin-waves can be easily calculated for a ferromagnetic phase and the obtained dispersion relation is exact for $U(1)$ invariant Hamiltonians like \hat{H} . This is an ideal situation for extracting the exchange and anisotropy parameters from the inelastic neutron measurements. To test the Hamiltonian (Eq. 1), we performed inelastic neutron scattering measurements above the second critical field, at $\mu_0H = 13.3$ T.

Spin-wave calculations predict the following one-magnon dispersion in a fully

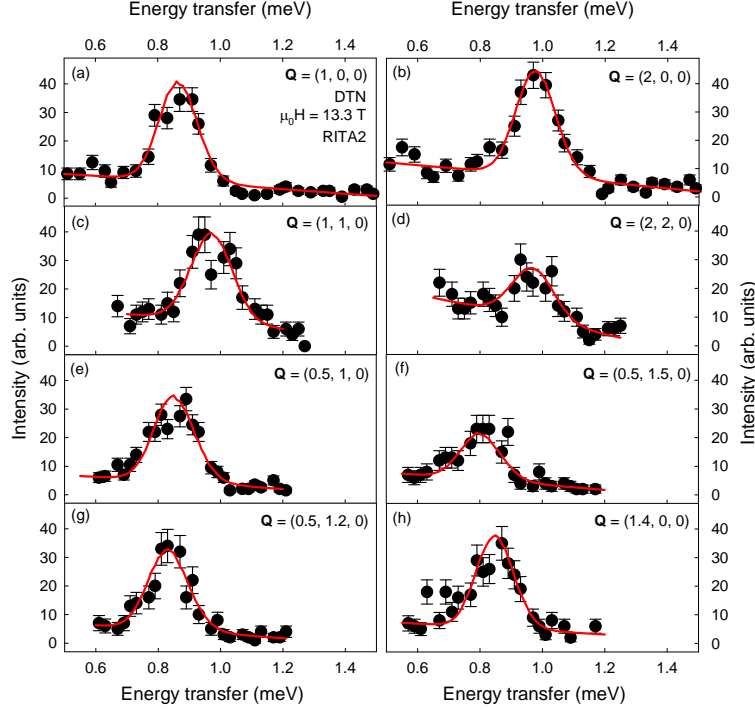


Figure 8. Energy scans performed in magnetic field $\mu_0H = 13.3$ T at $T < 50$ mK. The solid lines are fits of long-lived spin-wave excitations broadened by the resolution function.

saturated phase for the Hamiltonian (Eq. 1):

$$\begin{aligned}
 E_{\mathbf{Q}} = & g\mu_0H - D - 2\kappa(J_c + 2J_{ab}) - 8J_f \\
 & + 2[J_c \cos(2\pi l) + J_{ab} \cos(2\pi k) + J_{ab} \cos(2\pi h)] \\
 & + 8J_f \cos\left(\frac{2\pi h}{2}\right) \cos\left(\frac{2\pi k}{2}\right) \cos\left(\frac{2\pi l}{2}\right).
 \end{aligned} \tag{2}$$

For the Hamiltonian (Eq. 1), the second critical field H_{c2} is equal to

$$g\mu_B H_{c2} = D + 2(1 + \kappa)(J_c + 2J_a) + 8J_f. \tag{3}$$

Based on the Eq. 2, the interaction between two nickel sublattices, J_f , if present, can be determined as

$$J_f = \frac{1}{16}(E_{(2,0,0)} - E_{(1,0,0)}). \tag{4}$$

In a similar way the interaction between spins in ab -plane,

$$J_{ab} = \frac{1}{4}(E_{(0.5,1,0)} - E_{(0.5,1.5,0)}). \tag{5}$$

We investigated the dispersion of the low-lying magnetic excitation at $\mu_0H = 13.3$ T using the cold neutron three-axis spectrometer RITA2. Typical energy scans are shown in Fig. 8. The red lines are the result of a Gaussian convoluted with the instrument resolution function, indicating that the observed magnetic excitations are resolution-limited and long-lived.

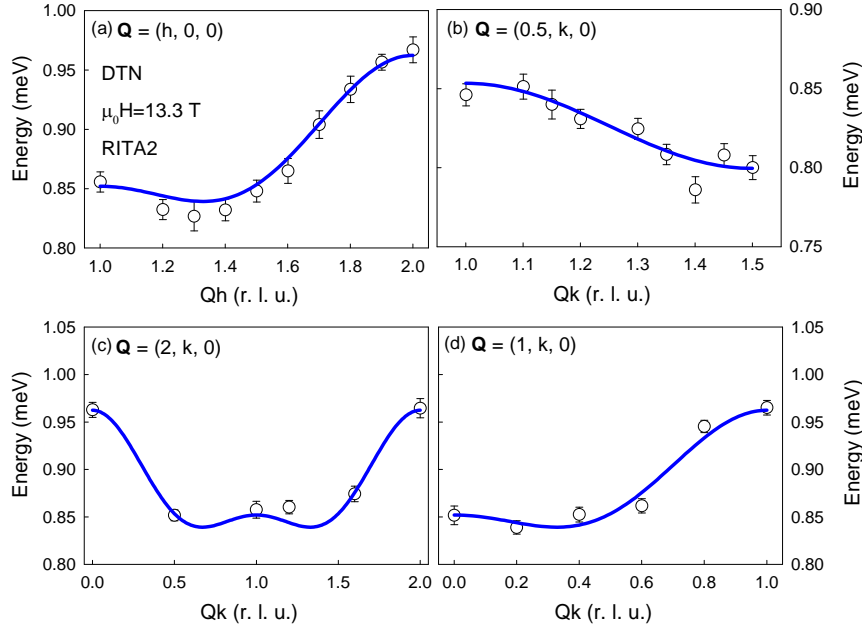


Figure 9. Dispersion of the low-lying magnon measured along different reciprocal directions in magnetic field $\mu_0 H = 13.3$ T at $T < 50$ mK. The blue lines show the spin-wave dispersion calculated based on the Eq. (2) and parameters given in the text.

The dispersion measured along $(h, 0, 0)$ direction, shown in Fig. 9(a), implies the presence of an exchange interaction between the corner and center spins. These measurements show that the magnon energy at $\mathbf{Q} = (2, 0, 0)$ and $\mathbf{Q} = (1, 0, 0)$ differ by $\delta E = 0.111(14)$ meV. According to Eq. 4, we therefore obtain the value $J_f = 0.08(1)$ K.

In order to obtain an independent estimate for J_{ab} , we performed constant Q -scans at $\mathbf{Q} = (0.5, 1, 0)$ and $\mathbf{Q} = (0.5, 1.5, 0)$, which are shown in Fig. 8 (e) and (f), respectively. The magnon energy changes by $\delta E \sim 0.054(14)$ meV between those two reciprocal vectors. According to Eq. (5), this corresponds to the exchange interaction in the ab -plane $J_{ab} = 0.156(4)$ K, which is in excellent agreement with an independent determination of $J_{ab} = 0.16$ K [12]. Using these exchange parameters and Eq. (2), we find good agreement between the dispersion measured along the $(0.5, k, 0)$ direction and the one calculated as shown in Fig. 9 (b).

The exchange interaction anisotropy, κ , and the easy-axis anisotropy, D , have the same wave-vector independent impact on the magnon energy. Therefore those parameters cannot be determined independently from our measurements. Assuming that $D = 8.9$ K, as determined from ESR measurements [20], the best agreement between the experimental data and the theoretical spin-wave dispersion is found for $\kappa = 1.01(1)$ (see Fig. 9).

Overall, we obtain the parameters $D = 8.9$ K, $J_c = 2.05$ K, $J_a = 0.156$ K, $J_f = 0.08$ K and $\kappa = 1.01$. The dispersion calculated using Eq. (2) with these parameters is shown in Fig. 9(a-d) for different directions in the reciprocal space, demonstrating

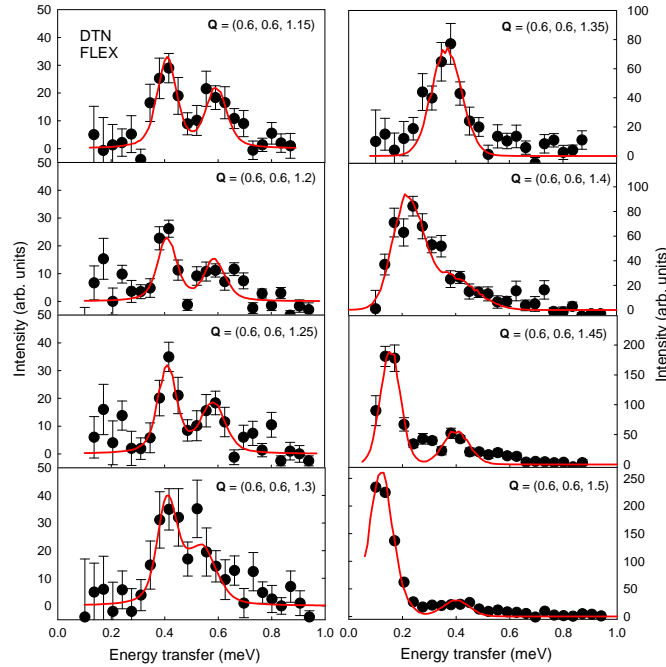


Figure 10. Energy scans performed along the $(0.6, 0.6, l)$ reciprocal direction in a magnetic field $\mu_0 H = 6$ T applied parallel to the tetragonal axis after the subtraction of the non-magnetic background. The measurements were done at $T < 50$ mK. The solid lines are fits of long-lived spin-wave excitations broadened by the resolution function.

excellent agreement with the experimental data. The second critical field calculated based on the Eq. (3) and the obtained parameters is equal to $\mu_0 H_{c2} = 12.6$ T, which is also in a good agreement with H_{c2} measured by specific heat, magnetocaloric and magnetization measurements [12, 13]. The proposed spin Hamiltonian (Eq. 1) with the parameters determined from our neutron spectroscopy experiment therefore provides a consistent description of the available macroscopic and spectroscopic data in the fully magnetized phase of $\text{NiCl}_2 \cdot 4\text{SC}(\text{NH}_2)_2$.

3.5. Spin dynamics deep in the AF phase

We also studied the spin dynamics in the AF phase of DTN using neutron spectroscopy. The measurements focused on energies below 1 meV, and thus track the development of the lower mode of the doublet into the ordered phase. We did not take measurements of the higher-lying doublet mode. Constant wave-vector and energy scans were performed along two directions at $\mu_0 H = 6$ T, namely $(h, h, 1.25)$ and $(0.6, 0.6, l)$. The choice of these wave-vectors resulted from the use of the horizontal-field magnet which restricted the access to the reciprocal plane of the sample. Background scattering was estimated from measurements with the sample rotated away from the magnetic scattering position.

Fig. 10 shows the energy scans at $\mu_0 H = 6$ T performed along $(0.6, 0.6, l)$ from $l = 1.15$ to $l = 1.5$ after the subtraction of the non-magnetic background. Energy

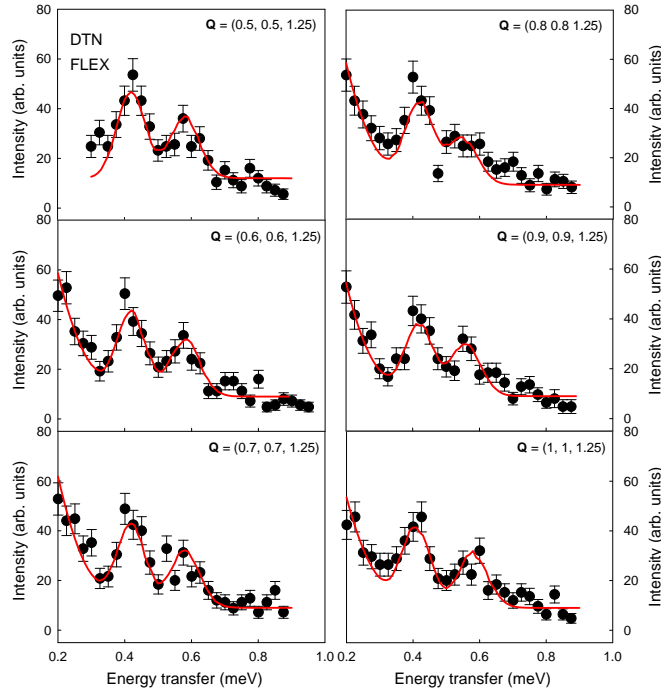


Figure 11. Energy scans along the $(h, h, 1.25)$ reciprocal direction performed in a magnetic field $\mu_0 H = 6$ T applied along tetragonal axis at $T < 50$ mK. The solid lines are fits of long-lived spin-wave excitations broadened by the resolution function.

scans along $(h, h, 1.25)$ from $h = 0.5$ to $h = 1$ are shown in Fig. 11. Two peaks are observed in both reciprocal directions, indicating a presence of two magnon modes at most wave-vectors. The data was fit to a model containing two Gaussians convoluted with the instrumental resolution function. The result is shown by the red lines in Fig. 10, showing that the observed peaks are resolution limited. The wave-vector dependence of the energies of two magnetic modes is shown in Fig. 12 for both reciprocal directions. In contrast to the excitations in the paramagnetic phase of DTN [12], the measurements in the AF phase at $\mu_0 H = 6$ T give clear evidence of a splitting of the lower doublet mode in the ordered phase into two modes, as shown in Fig. 12.

The detailed wave-vector dependence of the dispersion of the two observed modes is not very clear from our data, as one of the modes loses most of its intensity close to the AF point. There are two scenarios which are indicated by the solid lines in Fig. 12: 1) A strongly dispersive mode together with an essentially non-dispersive mode at about 0.42 meV, or 2) two dispersive modes with an anticrossing behaviour near $Q_L = 1.35$.

More detailed measurements at $\mu_0 H = 6$ T were done at low energies and directly at the wave-vector where the magnetic Bragg peaks are located. The corresponding dispersion is shown in Fig. 13. This allows a direct determination of the spin gap at this field. The observed dispersion can be described with a gap $\Delta E = 0.135(4)$ meV and a quadratic wave-vector dependence, suggesting the presence of the energy gap. The energy gap is comparable to that observed by ESR measurements [20], which is equal

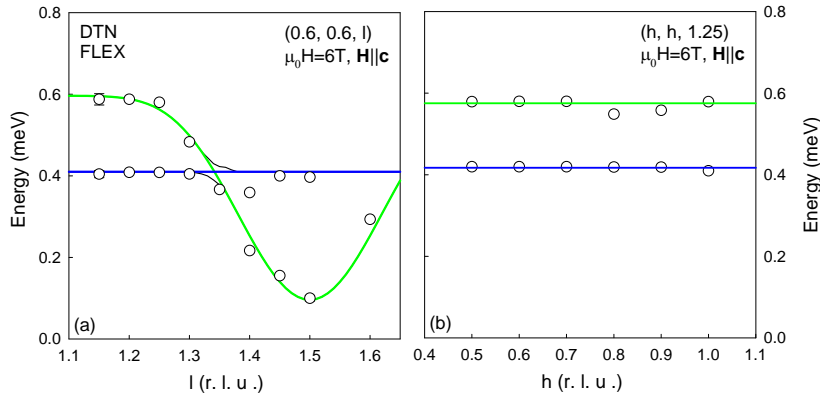


Figure 12. Magnetic dispersion of DTN for $T < 50$ mK, measured along the $(0.6, 0.6, l)$ and $(h, h, 1.25)$ reciprocal directions in a magnetic field $\mu_0 H = 6$ T applied parallel to the crystallographic c -axis, are shown in (a) and (b), respectively. The solid lines are guides to the eye and described in the text.

to $\Delta E \simeq 0.103$ meV.

The origin of the gap in the spectrum at $H = 6$ T and the splitting of the modes including their dispersion is not entirely clear. Sizanov and Syromyatnikov [21] have recently shown that the presence of an inter-sublattice exchange interaction such as J_f , which we directly demonstrated in this paper, will lead to a splitting of two degenerate magnon modes in an antiferromagnetically-ordered phase. The observation of two modes thus suggests that this has a strong effect on the spin dynamics in the ordered phase at 6 T. However, their calculations of the dispersion were done for relatively small D magnitudes where magnetic order is established at zero field, and there are a number of differences between their calculations and our observations: 1) They obtain a gapless mode, while the experiment gives evidence of two gapped modes. 2) The splitting of the two modes is much larger than predicted theoretically. 3) The dispersion we observe is relatively flat towards $l = 1$ while the predicted dispersion would have a cos-type wave-vector dependence in that wave-vector range. It is likely that higher-order terms of the magnon interaction lead to non-trivial corrections that can affect the dispersion of the magnetic excitations, and could at least partly resolve some of these differences.

There are a number of possible explanations for the differences between experiment and theory. One important aspect is of course that quantum fluctuations renormalize all the exchange interactions and the values of exchange interactions measured in the fully magnetized phase may be somewhat different for the AF state. This will lead to differences in the size of the splitting and of the predicted gap. However, the size of the splitting is far larger than could be expected from a renormalized J_f exchange interaction, and the presence of two gapped modes would not be affected by renormalized exchange interactions. We note that the excitations whose dispersion is shown in Fig. 12 have a much lower energy than the two-magnon bound state recently observed using ESR [22].

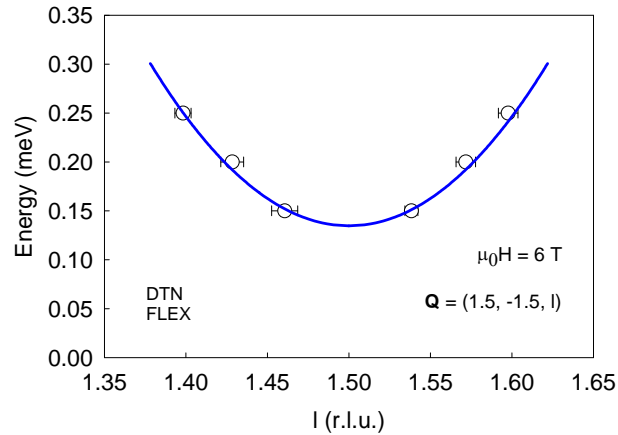


Figure 13. Low-energy part of the dispersion of low-lying excitation measured at $\mu_0 H = 6$ T applied parallel to the crystallographic c -axis and at $T < 50$ mK.

More important is however the effect of the strong anisotropy on the magnons. There are two magnetic ions in the unit cell that can give rise to differently polarized transverse spin-waves. In the absence of anisotropy, some of these modes will be degenerate. In the presence of a strong easy-axis anisotropy along the c -axis, as is this case here, it can be expected that the fluctuations along the c -axis will be much more costly than those in the basal plane, leading to a splitting. It is therefore likely that the strong anisotropy leads to an additional splitting, leading to three gapped modes in addition to a Goldstone mode. The ungapped mode would occur at the same wave-vector as the low-energy gapped mode, and would have been difficult to detect in our experiment. This scenario is consistent with the bulk of experiment on DTN which give evidence of an unbroken rotational symmetry at the BEC transition. In our experiment, we observe at least two of these gapped modes.

In addition, it is also possible that the magnetization of the sublattices at finite field could affect the spin dynamics in the ordered phase. The AF coupling of the two sublattices may change in the presence of sizeable ferromagnetically aligned neighbours belonging to different sublattices. Such a coupling may lead to a distortion of the crystal lattice and to additional interactions not present for $H < H_{c1}$ or $H > H_{c2}$, which could be responsible for the generation of the gap. The importance of spin-lattice coupling was also seen in ultrasonic measurements [23]. This interpretation is supported by magnetostriction measurements [15] that provide strong evidence for a coupling between the magnetic order and the lattice, and separate magneto-electric measurements which demonstrate the generation of electric polarization with increasing magnetic field [24, 19].

4. Summary

We studied the magnetism of the quantum $S = 1$ quasi-one-dimensional AF $\text{NiCl}_2 \cdot 4\text{SC}(\text{NH}_2)_2$ using neutron scattering. We characterized the field-induced magnetic order and the spin dynamics in the three phases, namely the quantum paramagnetic, field-induced AF and fully magnetized phases. Upon application of a magnetic field along the c -axis, we observe the splitting of a doublet state which condenses into the ground state at $H_{c1} = 2.1$ T. For $H_{c1} < H < H_{c2}$, we observed an antiferromagnetically ordered state with the moments aligned in the ab plane - perpendicular to the magnetic field direction. Our measurements confirm the picture of a BEC transition at H_{c1} .

The phase diagram of DTN was studied as a function of magnetic field and temperature. A dome-like shape of the HT phase diagram implies that thermal fluctuations prevent the system from magnetic order at higher temperatures. Our study of the magnetic phase diagram as a function of the angle γ between an applied magnetic field and the tetragonal axis shows the complete disappearance of the AF order above $\gamma \sim 55^\circ$. We also measured the one-magnon dispersion in the fully magnetized phase, at $\mu_0 H = 13.3$ T, leading to the direct observation of an inter-sublattice exchange interaction J_f . The spin dynamics in the AF phase shows the splitting of two magnon modes where J_f probably plays a crucial role. The study of the dispersion of the low-lying magnon in the AF phase of DTN reveal that there are at least two gapped magnons at $\mu_0 H = 6$ T.

While clearly establishing the presence of the J_f exchange interaction, the study also revealed several important open questions. Most importantly, the origin of at least two gapped magnons in the antiferromagnetically phase is not clear, and is probably the result of the strong easy-axis anisotropy that lifts the degeneracy of the transverse spin-waves, producing three gapped modes in addition to a Goldstone mode. Further experimental and theoretical work will be necessary to better understand the spin Hamiltonian in the AF phase.

5. Appendix

DTN crystallizes in the tetragonal $I4$ space group (#79) with the lattice parameters $a = 9.558$ Å and $c = 8.981$ Å. Nickel ions occupy $2a$ Wykoff positions belonging to the corners and the center of the chemical body-centered tetragonal unit cell. The magnetic unit cell has two nickel ions located at the positions $Ni_1 = (0, 0, 0 + z)$ and $Ni_2 = (0.5, 0.5, 0.5 + z)$, where z is equal to $z = -0.0894$.

The Laue class and the point group of DTN are $4/m$ and 4 , respectively. The space group $I4$ is non-centrosymmetric and has a lattice centering vector $\mathbf{C} = (0.5, 0.5, 0.5)$. For the body-centered space group $I4$, there is a general reflection condition for Bragg peaks $\mathbf{Q} = (h, k, l)$, which is $h + k + l = 2n$.

As the magnetic Bragg peaks were observed at $\mathbf{Q} = (0.5, 0.5, 0.5) \pm (h, k, l)$, where

	1	2_c
Γ_1	1	1
Γ_2	1	-1

Table 1. The character table and the irreducible representations obtained from group theory analysis for the tetragonal space group $I4$ (#79) and the magnetic ordering vector $\mathbf{k} = (0.5, 0.5, 0.5)$.

		Ni_1	Ni_2
Γ_1	$\vec{\phi}_1$	(0 0 1)	(0 0 -1)
Γ_2	$\vec{\phi}_2$	(1 0 0)	(-i 0 0)
	$\vec{\phi}_3$	(0 1 0)	(0 -i 0)

Table 2. Three basis vectors calculated for two nickel positions in primitive unit cell.

h , k and l are even numbers, the magnetic ordering vector is therefore $\mathbf{k} = (0.5, 0.5, 0.5)$. The magnetic ordering vector is invariant under two symmetry operations: the identity (1) and a two-fold rotation around the tetragonal axis (2_c). Therefore, there are two one-dimensional irreducible representations whose characters are summarized in the character table shown in Tab. 1.

\mathbf{Q}	$ F_{obs}(\mathbf{Q}) ^2$	$ F_{calc}(\mathbf{Q}) ^2$
(0.5, 0.5, 0.5)	33.34 (2.68)	9.53
(-0.5, 1.5, -0.5)	8.53 (6.79)	5.80
(1.5, 0.5, -0.5)	8.43 (1.43)	5.79
(1.5, -0.5, -0.5)	7.98 (1.18)	5.79
(1.5, 0.5, 0.5)	6.34 (1.11)	7.15
(-0.5, 1.5, 0.5)	7.89 (4.76)	7.15
(-1.5, 1.5, 0.5)	2.67 (1.63)	5.92
(1.5, 1.5, 0.5)	7.92 (3.22)	5.92
(2.5, 0.5, -0.5)	3.70 (1.00)	4.58
(2.5, -0.5, -0.5)	5.69 (1.62)	4.58
(2.5, 0.5, 0.5)	4.49 (0.89)	5.11
(2.5, 1.5, -0.5)	17.49 (5.10)	4.16
(1.5, 5.5, -0.5)	1.39 (0.14)	1.57
(-5.5, 5.5, 0.5)	1.58 (0.70)	0.58
(-2.5, 1.5, -0.5)	3.27 (1.00)	4.16
(2.5, -1.5, -0.5)	3.34 (1.02)	4.16
(-2.5, -1.5, -0.5)	4.09 (0.64)	4.16
(1.5, 5.5, 0.5)	1.12 (0.24)	1.54

Table 3. The observed and calculated magnetic structure factors for different wave-vectors. The quality of the fit is $\chi^2 = 4.89$.

The decomposition equation for the magnetic representation is $\Gamma_{mag} = 1\Gamma_1 + 2\Gamma_2$. The three basis vectors presented in Tab. 2 are calculated for the two nickel positions in a unit cell using the projection operator method acting on a trial vector ϕ_α

$$\Psi_{\alpha\nu}^\lambda = \sum_{g \in G_k} D_\nu^{\lambda*}(g) \sum_i \delta_{i,g_i} R_g \phi_\alpha \det(R_g),$$

where $\Psi_{\alpha\nu}^\lambda$ is the basis vector projected from the λ^{th} row of the ν^{th} irreducible representation, $D_\nu^{\lambda*}(g)$ is the λ^{th} row of the matrix representative of the ν^{th} irreducible representation for symmetry operation g , i denotes the atomic position and R_g is the rotational part of the symmetry operation g . The star of the propagation vector \mathbf{k} is formed by wave-vector $\mathbf{k}_1 = (0.5, 0.5, 0.5)$.

6. Acknowledgements

This work was supported by the DOE, the NSF and the Swiss National Science Foundation under Contract No. PP002-102831. A. P. F. acknowledges support from CNPq (Conselho Nacional de Desenvolvimento Científico e Tecnológico, Brazil). We thank HZB and ILL for the allocation of neutron radiation beam time. This work is partly based on experiments performed at the Swiss spallation neutron source SINQ, Paul Scherrer Institut, Villigen, Switzerland.

References

- [1] T. Giamarchi, C. Rüegg, and O. Tchernyshyov, *Nature Physics* **4**, 1745 (2008).
- [2] A. Oosawa, M. Ishii, and H. Tanaka, *Journal of Physics: Condensed Matter* **11**, 265 (1999).
- [3] T. Nikuni, M. Oshikawa, A. Oosawa, and H. Tanaka, *Phys. Rev. Lett.* **84**, 5868 (2000).
- [4] W. Shiramura *et al.*, *Journal of the Physical Society of Japan* **67**, 1548 (1998).
- [5] C. Rüegg *et al.*, *Phys. Rev. Lett.* **93**, 037207 (2004).
- [6] B. Grenier *et al.*, *Phys. Rev. Lett.* **92**, 177202 (2004).
- [7] M. Jaime *et al.*, *Phys. Rev. Lett.* **93**, 087203 (2004).
- [8] B. Grenier *et al.*, *Journal of Magnetism and Magnetic Materials* **310**, 1269 (2007).
- [9] V. O. Garlea *et al.*, *Phys. Rev. Lett.* **98**, 167202 (2007).
- [10] H.-T. Wang and Y. Wang, *Journal of Physics: Condensed Matter* **19**, 386227 (2007).
- [11] A. Lopez-Castro and M. R. Truter, *J. Chem. Soc.* 1309 (1963).
- [12] V. S. Zapf *et al.*, *Phys. Rev. Lett.* **96**, 077204 (2006).
- [13] A. Paduan-Filho, X. Gratens, and N. F. Oliveira, *Phys. Rev. B* **69**, 020405 (2004).
- [14] A. Paduan-Filho, X. Gratens, and J. Nei F. Oliveira, *J. Appl. Phys.* **95**, 7537 (2004).
- [15] V. S. Zapf *et al.*, *J. Appl. Phys.* **101**, 09E106 (2007).
- [16] L. Yin *et al.*, *Phys. Rev. Lett.* **101**, 187205 (2008).
- [17] F. Weickert *et al.*, *Phys. Rev. B* **85**, 184408 (2012).
- [18] S. A. Zvyagin *et al.*, *Phys. Rev. Lett.* **98**, 047205 (2007).
- [19] F. Weickert *et al.*, *Phys. Rev. B* **83**, 099901 (2011).
- [20] S. A. Zvyagin *et al.*, *Phys. Rev. B* **77**, 092413 (2008).
- [21] A. V. Sizanov and A. V. Syromyatnikov, *J. Phys.: Condens. Matter* **23**, 146002 (2011).
- [22] C. Psaroudaki *et al.*, *Phys. Rev. B* **85** 014412 (2012).
- [23] S. Zherlitsyn, *et al.*, *J. Phys. Conf. Ser.* **145**, 012069 (2009).
- [24] V. S. Zapf *et al.*, *Journal of Physics: Conference Series* **273**, 012132 (2011).